ISSN 2355-3286

Six-Axis Force–Torque Analysis of a Flexible-Tube Wrist for Misaligned Ports in Robotic EV Charging

Raihan Yusuf Rifansyah[1], Agus Heri Setya Budi[2], Hendri Maja Saputra[3]
[1, 2] Department of Electrical Engineering Education, Indonesia University of Education, Bandung, Indonesia
[1] raihanysf2013@upi.edu, [2] agusheri@upi.edu
[3] Research Center for Smart Mechatronics, National Research and Innovation Agency – BRIN, Bandung, Indonesia
[3] hend037@brin.go.id

Accepted on August 02, 2025
Approved on December 03, 2025

***Abstract* — As electric vehicle (EV) adoption accelerates, the demand for reliable autonomous charging systems in unstructured environments is growing. A critical challenge in these systems is achieving precise plug-port alignment, where vision-based methods often leave residual errors that can damage connectors. While passive compliance using flexible components is a promising solution, the complex contact mechanics of such materials under misalignment remain under-characterized. This paper presents a systematic 6-axis force-torque characterization of a flexible-tube wrist for robotic electric vehicle (EV) charging under various angular misalignments. Robotic plug insertion often relies on simplified models that fail to capture the complex contact dynamics of compliant mechanisms, limiting system robustness. To address this, we developed an experimental platform based on a cartesian robot with a roll–pitch–yaw wrist to measure full force–torque profiles during quasi-static insertions with controlled misalignments ranging from −8° to +8° in pitch and yaw. The results reveal a highly non-linear and asymmetric response, quantitatively demonstrated by a contact onset that shifts from a maximum depth of 45.8 mm at 0° to as early as 31.8 mm at +8° yaw, and peak axial forces reaching -18 N in pitch and -24 N in yaw. This asymmetry has practical implication, where a -5-degree pitch resulted in insertion failure while an equivalent +5-degree was successful. From this dataset, unique and repeatable force signatures were identified for each condition, providing a foundational basis for hybrid control strategies with force sensing to handle the final delicate insertion.**

***Index Terms*— Asymmetric Response; Robotic Charging; Compliant Mechanism; Flexible Tube; Force Measurement.**

I. INTRODUCTION

The growing adoption of electric vehicles (EVs) has driven intensive research on autonomous charging systems, which are essential for scalable, hands-free energy replenishment in future mobility ecosystems [1]. Unlike conventional fueling, EV charging requires precise plug insertion with minimal tolerance, making automation highly sensitive to alignment and contact quality. Characterizing force and torque dynamics is a critical step in designing compliant robotic systems, from industrial automation to wearable exoskeletons [2]. Consequently, various innovative architectures have been developed, including mobile or rail-mounted robotic chargers designed for structured environments such as parking garages [3].

Achieving precise alignment is challenging due to tight mechanical tolerances and the lack of standardized port geometries across vehicle models [1, 4]. Most approaches rely on vision-based systems using methods from deep learning to shape-based matching to detect the port location [4-6]. However, these systems have low robustness to environmental variations such as lighting and reflections [1, 4]. Studies show that even after seemingly successful vision-guided insertion, residual misalignments can persist, causing mechanical strain on the connector and port [4]. This underscores the need for complementary strategies for the final phase of plug insertion.

To address these residual errors, researchers incorporate compliance into the robotic systems, broadly classified into two approaches [7]. The first is active compliance, where force feedback actively modulates robot motion through algorithms such as impedance or admittance control [6, 8]. The second is passive compliance, which uses mechanical elements that deform upon contact to accommodate misalignment. Examples include elastic compensation units [9] or end-effectors with integrated flexible plugs [10]. However, flexible components introduce control challenges, notably complicating manipulator inverse kinematics [11].

Concurrently, other data-driven approaches have explored alternative sensing modalities to infer contact state or developed advanced learning-based control strategies for contact-rich tasks [12]. Research has shown the utility of Inertial Measurement Units (IMUs) to analyze vibration signals for the purpose of collision classification (determining if a contact is safe or unsafe)

[13] or for collision localization (estimating where on the port face contact occurred) [14]. Another novel approach involved developing the flexible tube itself into a sensor, using an embedded magnetic sensor and an LSTM network to predict interaction forces rather than measuring them directly [15].

However, despite numerous proposed control architectures and sensing modalities, the fundamental contact mechanics of a passively compliant plug, such as one made from thermoplastic polyurethane (TPU), under controlled angular misalignment remain uncharacterized. Understanding these force dynamics is essential for ensuring the long-term reliability, as uncontrolled insertion forces can cause mechanical wear, degradation, and eventual failure of the electrical connectors [16, 17]. To address this gap, this paper provides a systematic experimental characterization of the 6-axis forces and torques on a flexible-tube wrist. By directly measuring the force-position-torque response, we reveal nonlinearities and pronounced asymmetries that challenge simplified rigid-body models.

II. Materials and Methods

A. Experimental Platform

The experimental platform comprises three stepper-driven linear axes (X, Y, Z) mounted on a modular aluminum frame and controlled by an Arduino Uno with a CNC Shield. The vehicle-side charging port, a standard IEC 62196-2 receptacle with its electrical pins removed to isolate mechanical forces, is mounted on a fixture with manually adjustable pitch and yaw angles ranging from −8° to +8°. The plug is advanced linearly along the Z-axis to simulate an insertion under constant angular misalignment. For passive compliance, the plug is attached to the moving stage using a 3D-printed hollow tube. This component is the same unit previously validated in [15] and is fabricated from Thermoplastic Polyurethane (TPU) with a 95A Shore Hardness, 0% infill, and 1 mm wall thickness to allow elastic bending while effectively transmitting contact forces to the upstream sensor.

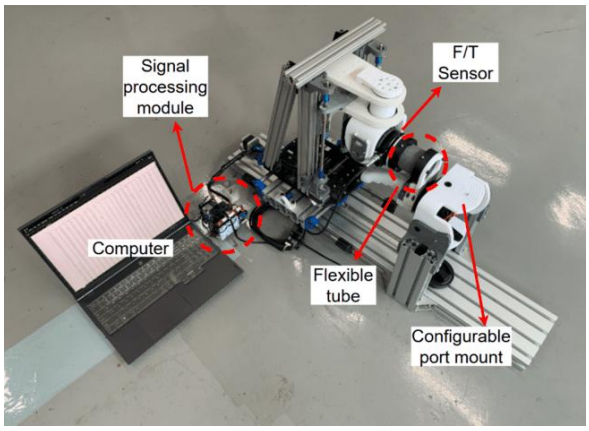

Fig. 1. Experimental Platform for Force–Torque Characterization of the Flexible-Tube Wrist Under Pitch and Yaw Misalignments.

The experimental platform, shown in Fig. 1, was constructed using a modular T-slot aluminum frame that forms the main base, Y-axis carriage, Z-axis column, and the configurable port mount structure. Nema 17 stepper motors drive all the three axes with T8 leadscrews equipped with anti-backlash nuts, while linear guidance is provided by LM13UU bearings. The majority of custom components, including motor mounts, bearing blocks, the port fixture, and the plug assembly, were fabricated from 3D-printed PLA+. The system is controlled by two Arduino Uno microcontrollers; the first uses a CNC Shield for motion control of the three stepper motors, while the second is dedicated to acquiring data from the F/T sensor. The two microcontrollers communicate via I2C to synchronize the force-torque data with the platform's position, which is then sent to a computer for data acquisition.

B. System Properties and Coordinate Frames

A right-hand coordinate frame centered at the base of the flexible tube is used for all analyses, as illustrated in Fig. 2. The X-axis represents the lateral motion (left/right) with pitch as rotation about this axis; the Y-axis represents the vertical motion (up/down) with yaw as rotation about this axis; and the Z-axis represents the insertion motion (forward/backward). Forces (Fx, Fy, Fz) and torques (Tx, Ty, Tz) are reported with respect to this coordinate frame.

The kinematic properties of the experimental platform include an operational workspace of 140 x 170 x 178 mm (X, Y, Z respectively). Platform motion is described by a kinematic model relating the actuator positions (joint space) to the end-effector's position (task space). The joint space vector is $q = [q_x, q_y, q_z]^T$, where each element corresponds to the linear displacement of a stepper-driven axis. The task space position vector is $P = [P_x, P_y, P_z]^T$. For this 3-DOF Cartesian manipulator, forward and inverse kinematics are given by the direct identity transformation $P = q$.

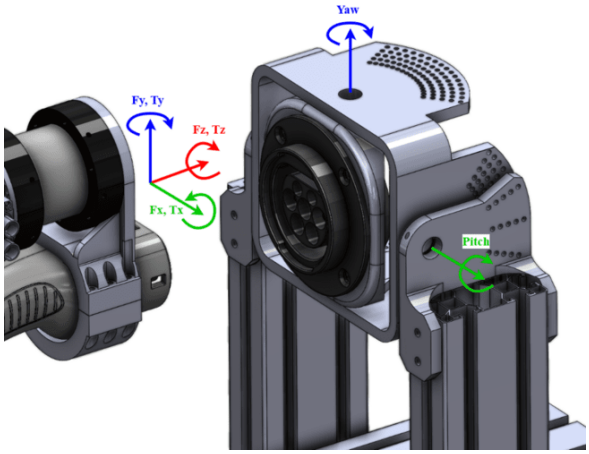

Fig. 2. Coordinate Frame Definitions for The Flexible-Tube Wrist, Indicating Lateral (X), Vertical (Y), and Axial (Z) axes.

C. Force-Torque Sensing and Data Acquisition

A six-axis force–torque sensor (AFT200, Aidin Robotics) is mounted between the moving carriage and the flexible tube. The sensor measures tri-axial force and torque data (Fx, Fy, Fz, Tx, Ty, Tz) with ranges of ±200 N and ±15 Nm and resolutions of 0.15 N and 0.015 Nm, respectively. Data is acquired via a CAN interface and synchronized with the platform position data. Because the flexible tube deforms during contact, the recorded Z-axis position represents the platform displacement and serves as a relative index of motion progression rather than the absolute plug-tip position.

D. Experimental Procedure

specific pitch or yaw angle. The plug was advanced at a constant low velocity along the Z-axis for a total travel distance of 70 mm to capture the entire contact event. The motion was considered quasi-static to minimize inertial effects, so that the measured forces primarily resulted from elastic deformation. This procedure was repeated 10 times for each of the 17 angular offsets (from −8° to +8° in 1° increments) for both pitch and yaw. All data collection was conducted in an open-loop, feedforward manner without active feedback control or external pose tracking.

A total travel distance of 70 mm was selected to ensure that the entire insertion process was fully captured under all misalignment conditions. Preliminary tests indicated that initial contact occurred as late as 45.8 mm for the 0° configuration and as early as 31.8 mm for ±8°; therefore, a shorter travel range would risk failing to reach the final seating or failure region, which typically emerges around 55–60 mm. Extending the travel to 70 mm provides a sufficient margin to observe the complete progression of events from free-space motion, through initial impact and continuous elastic deformation, to the final resting state. This margin ensures that no critical interaction or steady-state behavior is truncated while remaining within the safe bending limits of the flexible tube.

E. Data Processing and Analysis

The analysis focused on the 30–60 mm segment of the insertion path, where the main contact events occurred. Key metrics were extracted from the averaged data of 10 repeated trials for each condition. Contact onset was identified by manual visual inspection of the force-torque profiles, chosen instead of a global automated threshold to better handle variations in initial contact behavior. Onset was defined as the position where the profiles first showed a clear and sustained deviation from the baseline noise.

For the quantitative trend analysis, a critical mechanical event was identified for each trial instead of relying on simple peak values. This event represented the point of maximum mechanical resistance, typically determined by the primary peak in axial force (Fz) or a sharp change in the slope of vertical force (Fy). The 6-axis force-torque vector was extracted at this event position to construct a composite force signature for each misalignment condition. Finally, these signatures were used to analyze trends across all angular conditions, assessing nonlinearity, asymmetry, and cross-axis coupling.

III. Result and Discussion

The experimental data revealed complex, repeatable, and highly asymmetric force-torque profiles that are characteristic of each angular misalignment conditions. These profiles, or force signatures, provide a detailed representation of the mechanical interactions during the insertion process. The following sections present the pitch and yaw signatures, followed by a quantitative analysis of key trends.

The initial analysis examines the three primary force components generated during pitch misalignment. Fig. 3 shows the averaged force profiles for lateral (Fx), vertical(Fy), and axial (Fz) components as a function of insertion position across the full range of negative and positive pitch angles.

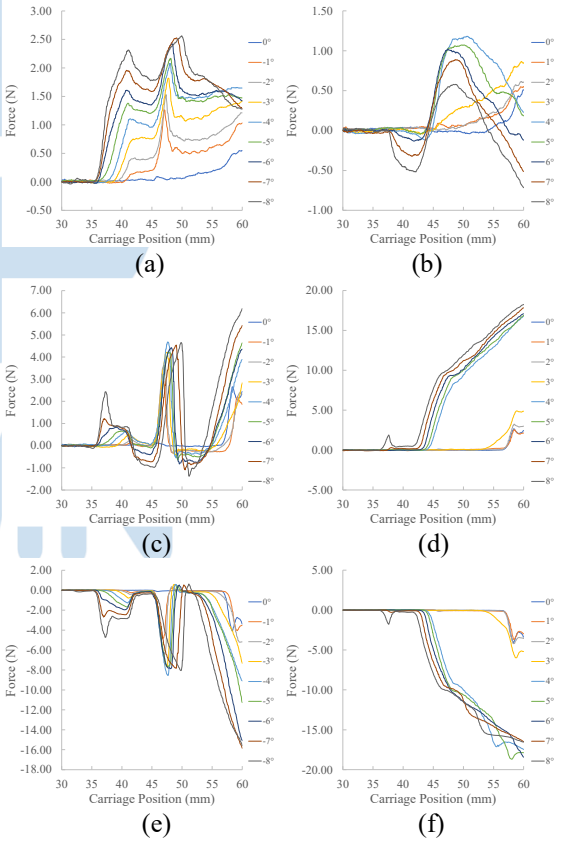

Fig. 3. Force Profiles for Pitch Misalignment Across Insertion Positions: (a) Fx for negative pitch; (b) Fx for positive pitch; (c) Fy for negative pitch; (d) Fy for positive pitch; (e) Fz for negative pitch; and (f) Fz for positive pitch.

The force profiles in Fig. 3 show clear asymmetry between negative and positive pitch. Negative pitch condition (Fig. 3a, 3c, 3e) produces complex, multi-stage contact dynamic with a distinct dual-peak signature in the vertical (Fy) and axial (Fz) forces, indicating stick-slip or jamming. In contrast, the positive pitch condition (Fig. 3b, 3d, 3f) yields

smoother, monotonic force curves but with a higher vertical reaction force (Fy), indicating a more monotonic but high-friction sliding contact.

To complement the force analysis, the torque profiles for pitch misalignment were examined. Fig. 4 displays the three primary torque components, providing insight into the rotational dynamics.

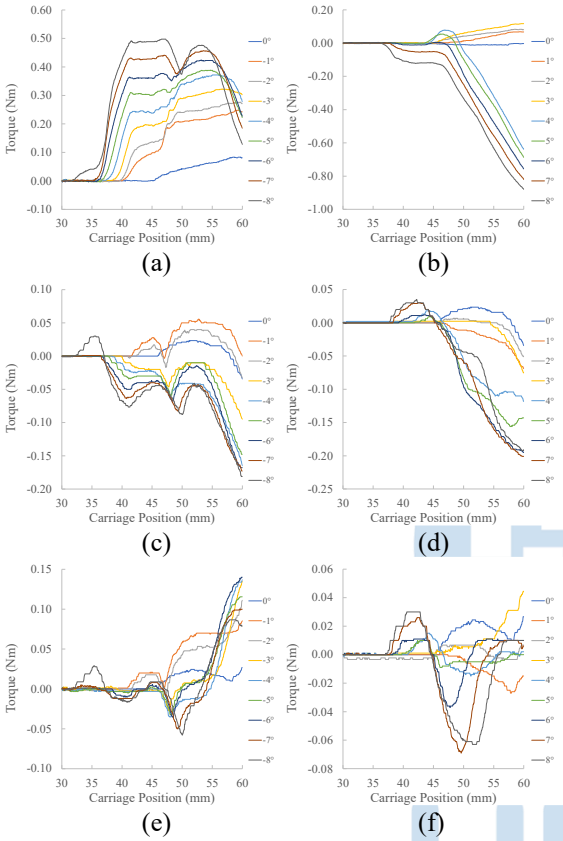

Fig. 4. Torque Profiles for Pitch Misalignment, Highlighting Polarity Reversal and Bending Loads: (a) Tx for negative pitch; (b) Tx for positive pitch; (c) Ty for negative pitch; (d) Ty for positive pitch; (e) Tz for negative pitch; and (f) Tz for positive pitch.

The asymmetry is further detailed in the torque profiles shown in Fig. 4. The primary bending torque (Tx) is a strong directional indicator, showing a complete polarity reversal between negative (Fig. 4a) and positive (Fig. 4b) pitch. Notably, the peak torque magnitude is substantially larger for positive pitch, indicating a greater bending load is imparted on the flexible tube. The secondary and third torques (Ty and Tz) confirm a complex 3D interaction involving both lateral bending and twisting.

The investigation was extended to yaw misalignment. Fig. 5 shows the averaged force profiles for the lateral (Fx), vertical (Fy), and axial (Fz) components under controlled negative and positive yaw deviations, revealing a distinctly different mechanical response compared with pitch.

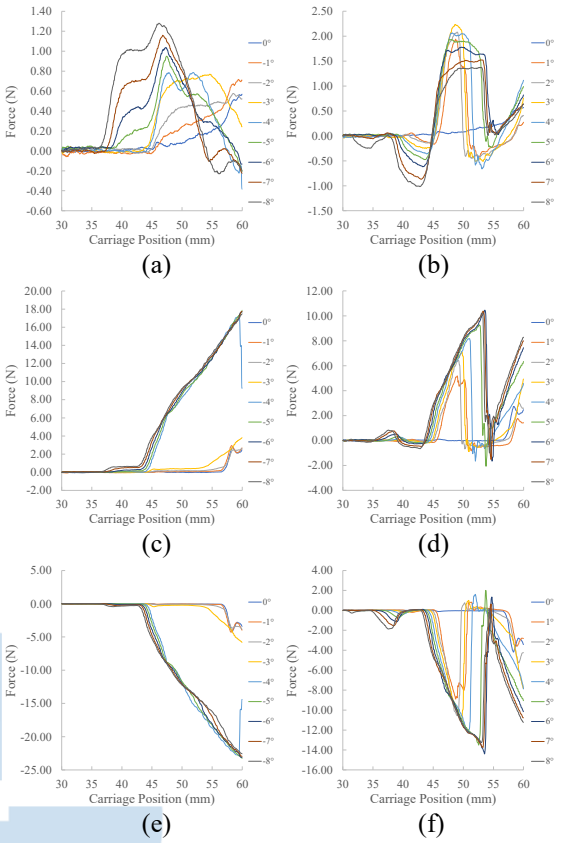

Fig. 5. Force Profiles for Yaw Misalignment Under Positive and Negative Deviations: (a) Fx for negative yaw; (b) Fx for positive yaw; (c) Fy for negative yaw; (d) Fy for positive yaw; (e) Fz for negative yaw; and (f) Fz for positive yaw.

The force profiles in Fig. 5 indicate that the response to positive yaw is significantly more complex and irregular than negative yaw. Under positive yaw, the lateral force (Fx) exhibits a distinct force reversal, beginning with a negative peak as the plug tip makes initial contact with one side of the port flange, followed by a much larger positive peak as it slides and presses against the opposite side. This complex interaction is also reflected in the vertical(Fy) and axial (Fz) forces, which are characterized by sharp transient events and abrupt reversals indicative of a stick-slip dynamic. In contrast, negative yaw (Fig. 5a, 5c, 5e) produces a more predictable and monotonic response, notably in the large coupled vertical (Fy) and axial (Fz) forces, which increase smoothly without the sharp fluctuations observed in the positive yaw condition.

The rotational dynamics under yaw misalignment were analysed by examining the three corresponding torque components. Fig. 6 shows the three primary torque components, providing insight into the rotational dynamics.

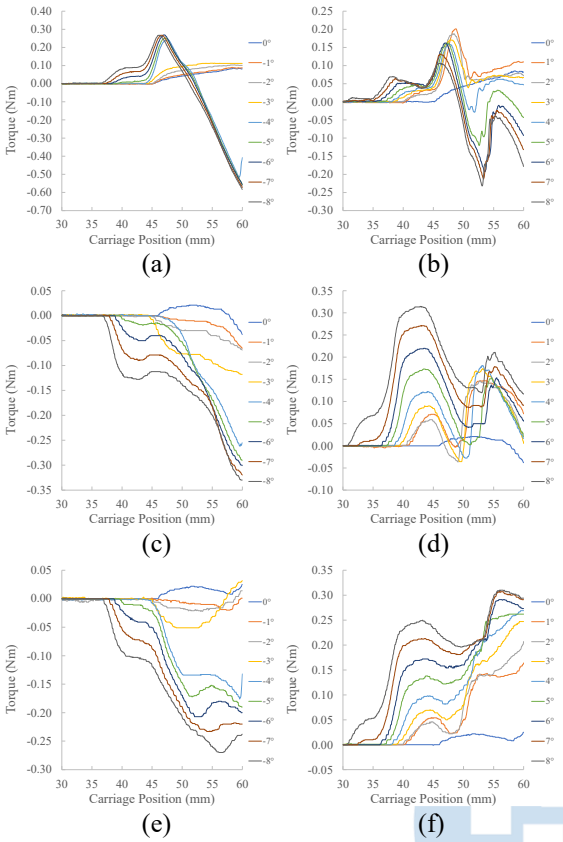

Fig. 6. Torque Profiles for Yaw Misalignment, Showing Strong 3D Coupling Effects: (a) Tx for negative yaw; (b) Tx for positive yaw; (c) Ty for negative yaw; (d) Ty for positive yaw; (e) Tz for negative yaw; and (f) Tz for positive yaw.

The torque profiles in Fig. 6 provide further insight into the rotational dynamics of yaw misalignment. For the primary bending torque (Tx), negative yaw (Fig. 6a) shows two distinct behaviours: for small angles, the torque remains consistently positive, whereas for larger angles, the response transitions to a positive peak followed by a smooth, monotonic reversal into a negative value. In contrast, all positive yaw angles (Fig. 6b) generate a high-gradient, non-monotonic profile, characterized by an initial positive peak that is immediately followed by a sharp reversal to a negative trough, before ending in a fluctuating state. This behaviour suggests a more severe interaction involving phenomena such as snap-through buckling or intermittent slip-stick contact. Lastly, the lateral torque (Ty) and twisting torque (Tz) emerge as highly reliable indicators of yaw direction, exhibiting a clear and systematic polarity reversal between negative and positive angles.

A. Quantitative Analysis of the Contact Onset

To quantify and summarize the observed behaviors, key metrics were extracted from the profiles. Fig. 7 plots the initial contact onset position as a function of the misalignment angle. Both pitch and yaw show a distinct arch-shaped profile, where contact occurs latest near 0° and progressively earlier towards the ±8° extremes. The plot also provides a clear quantitative measure of asymmetry; both profiles are asymmetric, with yaw showing a more pronounced overall difference compared to pitch.

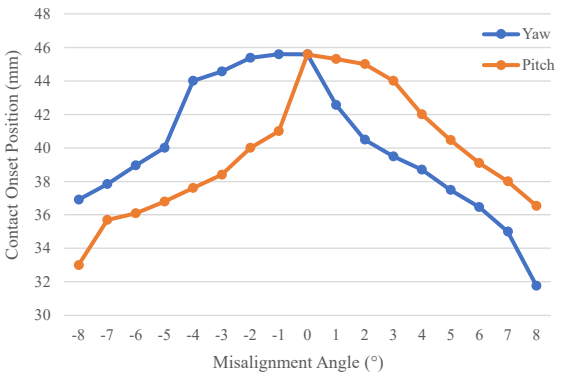

Fig. 7. Contact Onset Position as a Function of Misalignment Angles for Pitch and Yaw.

Fig 7 compares contact onset position versus of the misalignment angle for pitch and yaw. Both exhibit an arch-shaped profile, with contact occurring latest (deepest into the insertion path) near the 0° and progressively earlier as the misalignment increases towards the ±8°. The figure clearly shows that the pitch and yaw profiles differ in both shape and magnitude.

The arch-shaped trend is intuitive because a greater initial tilt causes the plug's leading edge to engage with the port chamfer earlier in its forward travel. More importantly, the plot provides a quantitative measure of asymmetry for both axes. The yaw profile is highly asymmetric, with positive yaw angles producing different onset positions than negative ones. The pitch profile also shows asymmetry, as contact at +8° occurs at a distinctly different position than at -8°. These results indicate that the initial contact dynamics depend on misalignment direction for both pitch and yaw, which is a critical insight for predictive control model development.

B. Quantitative Analysis of the Primary Mechanical Event

Further analysis was conducted by identifying the position of the primary mechanical event, which corresponds to the moment of maximum resistance in each trial. Unlike a simple maximum value search, the position of this event was determined for each angle through manual visual inspection to accurately capture its specific characteristics. This critical event was identified by distinct features in the profiles, such as a transient reversal with the highest magnitude or a significant change in the slope of a primary force component within a specific range of travel. By defining the event based on these physical phenomena rather than a simple peak, a more consistent and meaningful comparison across different misalignment conditions could be achieved. The 6-axis force-torque vector was then extracted at this identified event position for subsequent quantitative analysis.

Fig. 8 illustrates how this event positions shift along the insertion path. The plot reveals at least two distinct mechanical regimes both for pitch and yaw: the event occurs very late for small angles but shifts to a much earlier position for larger angles, indicating a fundamental change in contact mode.

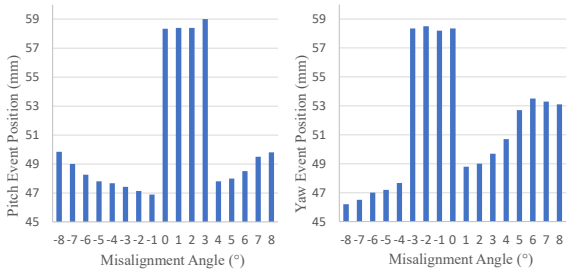

(a) (b)

Fig. 8. Position of the primary mechanical event as a function of pitch and yaw misalignment: (a) Event position for pitch; and (b) Event position for yaw.

The primary mechanical event position shifts along the insertion path as a function of the pitch and yaw misalignment angles as shown in Fig. 8. The data reveal a distinct, non-uniform pattern both for pitch and yaw, where the event occurs late in the path for small angles (0° to +3°) for pitch and (-3° to 0°) for yaw but shifts to a much earlier position for larger angles."

The large shift in the event position suggests the presence of two distinct mechanical regimes. For small misalignments, the system operates in a compliance zone, where no hard jamming occurs and the maximum force results from friction building up near the end of insertion. For larger misalignments, the system enters a hard contact zone, where a distinct earlier mechanical event, likely jamming or high-stress bending, becomes the dominant feature. The yaw response asymmetry further indicates that the regime transition depends on misalignment direction.

To quantify the system asymmetry and sensitivity, the magnitudes of the three primary force components were extracted at each event position. Fig. 9 presents these force values as functions of misalignment angle for both pitch and yaw.

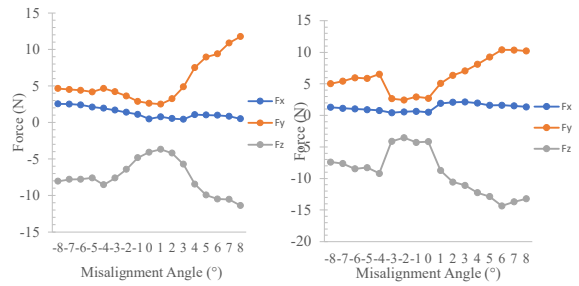

(a) (b)

Fig. 9. Force Event as a Function of Misalignment Angle: (a) Force event for pitch; and (b) Force event for yaw.

Fig. 9 summarizes the event force magnitudes for the Fx, Fy, and Fz, extracted at the primary mechanical event for both pitch and yaw. The plot shows the nonlinear relationship between misalignment angle and the resulting reaction forces.

This plot provides the strongest quantitative evidence of the system force asymmetry. The pitch analysis (Fig. 9a) shows distinct trend in dominant forces (Fy and Fz) for negative and positive angles. The yaw analysis (Fig. 9b) is even more pronounced: negative yaw is dominated by a large coupled vertical force (Fy), while positive yaw is dominated by a much larger primary lateral force (Fx). These results confirm that the nature of mechanical resistance fundamentally differs depending on yaw direction.

Finally, to complete the quantitative analysis, the torque events were extracted at the mechanical event. Fig. 10 presents the corresponding torque magnitudes for the three rotational components (Tx, Ty, Tz) extracted at the primary mechanical event. The plot illustrates the sensitivity and directional nature of the torque response.

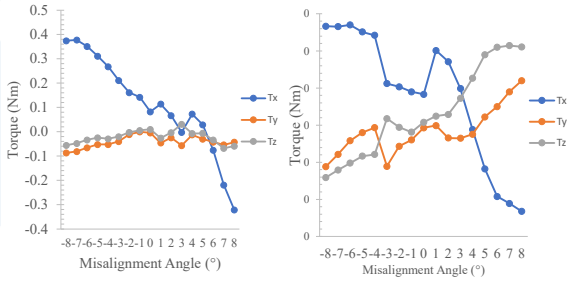

(a) (b)

Fig. 10. Torque Event as a Function of Misalignment Angle: (a) Torque event for pitch; and (b) Torque event for yaw.

The torque event analysis identifies the components that best indicate direction. For pitch misalignment (Fig. 10a), the primary bending torque (Tx) demonstrates a clear and consistent polarity reversal, with positive values for negative pitch and negative values for positive pitch. Similarly, for yaw misalignment (Fig. 10b), the lateral (Ty) and twisting (Tz) torques also show a perfect polarity reversal, making them reliable indicators for sensor-based control. The complex, non-monotonic behaviour of the other torque components further confirms strong and unpredictable 3D coupling effects.

C. Qualitative Validation of Final Plugging States

To provide qualitative validation and link quantitative data with physical outcomes, final plugging states were visually documented for representative misalignment angles. This visual inspection confirms whether insertion was successful or failed under different conditions.

The final plugging states for key pitch misalignment angles are presented first. Fig. 11 shows a side-view comparison for -5°, 0°, and +5° pitch angles to illustrate the system's functional asymmetry

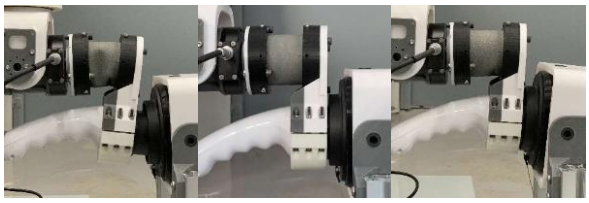

(a) (b) (c)

Fig. 11. Final Plugging State for Pitch Misalignment: (a) -5°; (b) 0°; and (c) +5°.

As shown in Fig. 11, a clear correlation between the force signatures and the insertion is evident. For the 0° condition (Fig. 11b), the plug is perfectly seated, matching the observed low-force profiles. At a +5° pitch misalignment (Fig. 11c), the system's passive compliance accommodates the error, allowing a complete insertion.

A key finding is the functional asymmetry shown in this comparison. While +5° misalignment results in a successful insertion, -5° misalignment causes insertion failure, where the plug is visibly canted and cannot be fully seated (Fig. 11a). This failure directly corresponds to the irregular dual-peak force profile observed for negative pitch, confirming it as a more challenging condition and defining an operational limit for the passive compliance mechanism.

Next, the final plugging states for key yaw misalignment angles were documented. Fig. 12 compares the outcomes for the extreme angles of -8° and +8°, with the 0° condition as a baseline.

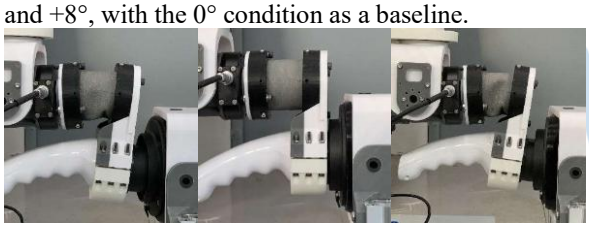

(a) (b) (c)

Fig. 12. Final Plugging State for Yaw Misalignment: (a) -8°; (b) 0°; and (c) +8°.

As shown in Fig. 12, the 0° condition (Fig. 12b) again serves as a baseline for a successful insertion. However, the outcomes at the extreme angles of -8° (Fig. 12a) and +8° (Fig. 12c) both resulted in insertion failure, where the plug became canted and could not be fully seated. This demonstrates that while the system can accommodate moderate yaw deviations, its operational limit is exceeded at these extreme angles.

A closer analysis of the failure modes reveals subtle differences between the two conditions. The final canted state at +8° yaw appears more severe or misaligned compared to the -8° condition. This visual evidence reinforces the quantitative findings that the underlying mechanical stresses and irregular dynamics are significantly greater for positive yaw. This underscores that not only the success of the insertion, but also the nature of the failure can vary significantly depending on the direction of misalignment.

D. Interpretation of Asymmetric Contact Mechanics

The pronounced asymmetry observed in both force and torque responses is a key finding of this study. It results from the complex interaction between the compliant tube's deformation and the plug-port interface geometry. Different contact points on the port's chamfer for positive and negative angles cause the plug to bend and twist in distinct ways. This is quantitatively confirmed in the event force analysis (Fig. 9), where negative yaw is dominated by a large coupled vertical force (Fy), while positive yaw produces a much larger primary lateral force (Fx). This difference in force magnitudes and dynamic stability is visually confirmed by the qualitative validation (Fig. 11), where a -5° pitch results in a insertion failure (canting), while a +5° pitch leads to a successful insertion. Furthermore, the existence of strong cross-axis coupling, such as the significant vertical force (Fy) generated during horizontal yaw misalignment, underscores that the interaction is an inherently 3D phenomenon that cannot be adequately described by simpler, 2D rigid-body models.

E. The Force Signature Concept and Implications for Control

The distinct and repeatable nature of the 6-axis profiles for each misalignment condition gives rise to the concept of a unique force signature. Each signature, defined by the instantaneous 6-axis force-torque vector at the primary mechanical event, acts as a mechanical fingerprint containing rich information about the state of contact, as quantitatively demonstrated by the unique component magnitudes (Fig. 9, Fig. 10) and event timing (Fig. 8) for each angle. This finding has significant implications for a hybrid control strategy; for example, the signature for a -5° pitch, which leads to insertion failure, is fundamentally different from that of a +5° pitch, which results in success. While a vision system can handle the initial coarse alignment, these force signatures are invaluable for the final, delicate insertion phase. By recognizing characteristic features within a signature, a control algorithm could diagnose the direction, approximate magnitude, and even the potential outcome of an insertion error in real-time, providing a strong basis for robust, adaptive force-guided controllers that can react intelligently to specific conditions.

IV. CONCLUSION

This study presents a systematic characterization of six-axis force and torque responses from a flexible-tube wrist under pitch and yaw misalignments ranging from −8° to +8°. The results reveal a non-linear and directionally asymmetric mechanical behavior, which was found to be both quantitative and functional. For

instance, a -5° pitch misalignment resulted in insertion failure, whereas an equivalent +5° was successful. Key quantitative findings include a contact onset that shifts from a maximum depth of 45.8 mm at 0° to as early as 31.8 mm at +8° yaw, and peak final plugging state axial forces (Fy) reaching -18 Newtons in pitch and -24 Newton in yaw. A key contribution is the identification of unique and repeatable force signatures for each misalignment condition. These patterns provide a foundation for developing more robust, adaptive control strategies in autonomous EV charging systems.

Initial attempts to create a validating finite element model were unsuccessful, as the nonlinear analysis in SolidWorks Simulation consistently failed to converge due to the large deformations and geometric nonlinearity of the thin-walled TPU component. A successful quantitative validation is therefore a key direction for future work, requiring a more sophisticated approach with advanced solvers such as arc-length or Riks methods, combined with a calibrated hyperelastic material model. The ultimate goal is to leverage the dataset presented here to train a machine-learning model for a hybrid alignment strategy. This approach would use a vision system for coarse localization of the charging port before transitioning to a force-guided control mode, which would use the identified signatures to correct residual errors during the final, delicate insertion phase, combining the strengths of both sensing modalities for a highly robust system.

REFERENCES

[1] H. M. Saputra, N. S. M. Nor, E. Rijanto, M. Z. Md Zain, I. Z. Mat Darus, and E. Yazid, "A review of robotic charging for electric vehicles," *International Journal of Intelligent Robotics and Applications,* vol. 8, no. 1, pp. 193-229, 2024, doi: 10.1007/s41315-023-00306-x.

[2] D. Rodríguez Jorge, J. Bermejo García, A. Jayakumar, R. Lorente Moreno, R. Agujetas Ortiz, and F. Romero Sánchez, "Force and Torque Characterization in the Actuation of a Walking-Assistance, Cable-Driven Exosuit," *Sensors*, vol. 22, no. 11, doi: 10.3390/s22114309.

[3] A. Hu *et al.*, "SkyvoltRobot: A Novel Rail-Mounted Charging Robot for Electric Vehicles," *Procedia Computer Science,* vol. 250, pp. 274-281, 2024, doi: https://doi.org/10.1016/j.procs.2024.11.036.

[4] J. Miseikis, M. Rüther, B. Walzel, M. Hirz, and H. Brunner, "3D Vision Guided Robotic Charging Station for Electric and Plug-in Hybrid Vehicles," 2017, doi: 10.48550/arXiv.1703.05381.

[5] P. Quan, Y. Lou, H. Lin, Z. Liang, and S. Di, "Research on Fast Identification and Location of Contour Features of Electric Vehicle Charging Port in Complex Scenes," *IEEE Access,* vol. 10, pp. 26702-26714, 2022, doi: 10.1109/ACCESS.2021.3092210.

[6] P. Sun *et al.*, "Research on autonomous positioning and adaptive compliant plugging strategies of intelligent charging robots," *Computers in Industry,* vol. 168, p. 104287, 2025, doi: https://doi.org/10.1016/j.compind.2025.104287.

[7] M. Zhu, D. Gong, Y. Zhao, J. Chen, J. Qi, and S. Song, "Compliant Force Control for Robots: A Survey," *Mathematics*, vol. 13, no. 13, doi: 10.3390/math13132204.

[8] H. Zhang, W. Zhu, and Y. Huang, "A research on the control strategy of automatic charging robot for electric vehicles based on impedance control," *Journal of Physics: Conference Series,* vol. 2303, no. 1, p. 012085, 2022, doi: 10.1088/1742-6596/2303/1/012085.

[9] J. Bucher, J. Knipschild, and B. Künne, "Development and evaluation of an automatic connection device for electric cars with four DOFs and a control scheme based on infrared markers," *International Journal of Mechatronics and Automation,* vol. 8, p. 1, 01/01 2021, doi: 10.1504/IJMA.2021.10043805.

[10] Y. Lou and S. Di, "Design of a Cable-Driven Auto-Charging Robot for Electric Vehicles," *IEEE Access,* vol. 8, pp. 15640-15655, 2020, doi: 10.1109/ACCESS.2020.2966528.

[11] H. M. Saputra, R. Y. Rifansyah, C. H. A. H. B. Baskoro, N. S. M. Nor, E. Rijanto, and A. Pahrurrozi, "Comparative Study of Machine Learning Models for Inverse Kinematic Prediction of a Flexible-Tube Wrist Mechanism in Robotic Charging Stations," in *2024 IEEE International Conference on Smart Mechatronics (ICSMech)*, 19-21 Nov. 2024, pp. 152-158, doi: 10.1109/ICSMech62936.2024.10812340.

[12] Y. Wang, C. C. Beltran-Hernandez, W. Wan, and K. Harada, "An Adaptive Imitation Learning Framework for Robotic Complex Contact-Rich Insertion Tasks," *Frontiers in Robotics and AI,* Original Research vol. 8 - 2021, 2022. [Online]. Available: https://www.frontiersin.org/journals/robotics-and-ai/articles/10.3389/frobt.2021.777363.

[13] H. Lin, P. Quan, Z. Liang, D. Wei, and S. Di, "Enhancing Safety in Automatic Electric Vehicle Charging: A Novel Collision Classification Approach," *Applied Sciences*, vol. 14, no. 4, doi: 10.3390/app14041605.

[14] H. Lin, P. Quan, Z. Liang, Y. n. Lou, D. Wei, and S. Di, "Precision Data-Driven Collision Localization with a Dedicated Matrix Template for Electric Vehicle Automatic Charging," *Electronics*, vol. 13, no. 3, doi: 10.3390/electronics13030638.

[15] H. Saputra *et al.*, "Three-axis flexible tube sensor with LSTM-based force prediction for alignment of electric vehicle charging ports," *Journal of Mechatronics, Electrical Power, and Vehicular Technology,* vol. 15, pp. 208-219, 12/31 2024, doi: 10.55981/j.mev.2024.1104.

[16] Y. Meng and W. Ren, "Investigation on failure mechanism of electrical connectors under repetitive mechanical insertion and withdrawal operations," *IOP Conference Series: Materials Science and Engineering,* vol. 1207, no. 1, p. 012011, 2021, doi: 10.1088/1757-899X/1207/1/012011.

[17] L. Xu, S. Ling, and D. Li, "Insertion force quality consistency investigation of electrical connector," in *2016 IEEE 11th Conference on Industrial Electronics and Applications (ICIEA)*, 5-7 Jun. 2016, pp. 2395-2399, doi: 10.1109/ICIEA.2016.7603994.